Tictoid Expanded Pyridiniums: Assessing Structural, Electrochemical, Electronic, and Photophysical Features

11 AUTHORS, INCLUDING:

Adrian Calborean
National Institute for Research and Developm…
25 PUBLICATIONS **147** CITATIONS

Fethi Bedioui
French National Centre for Scientific Research
264 PUBLICATIONS **6,450** CITATIONS

Fausto Puntoriero
Università degli Studi di Messina
107 PUBLICATIONS **2,763** CITATIONS

Philippe P Lainé
Paris Diderot University
46 PUBLICATIONS **1,320** CITATIONS

Tictoid Expanded Pyridiniums: Assessing Structural, Electrochemical, Electronic, and Photophysical Features

Jérôme Fortage,[†] Fabien Tuyèras,[†] Cyril Peltier,[‡] Grégory Dupeyre,[†] Adrian Calboréan,[‡,§] Fethi Bedioui,[∥] Philippe Ochsenbein,[⊥] Fausto Puntoriero,[#] Sebastiano Campagna,*[,#] Ilaria Ciofini,*[,‡] and Philippe P. Lainé*[,†]

[†]Université Paris Diderot, Sorbonne Paris Cité, ITODYS, UMR 7086 CNRS, 15 rue Jean-Antoine de Baïf, 75013 Paris, France

[‡]École Nationale Supérieure de Chimie de Paris − Chimie ParisTech, LECIME, UMR 7575 CNRS, 11 rue Pierre et Marie Curie, 75005 Paris, France

[§]Department of Molecular and Biomolecular Physics, National Institute for Research and Development of Isotopic and Molecular Technologies, 65-103 Donath Str., Ro-400293 Cluj-Napoca, Romania

[#]Dipartimento di Chimica Inorganica, Chimica Analitica e Chimica Fisica, Università di Messina, and Centro Interuniversitario per la Conversione Chimica dell'Energia Solare (SOLARCHEM), Via Sperone 31, I-98166 Messina, Italy

[∥]Laboratoire de Pharmacologie Chimique et Génétique et d'Imagerie, Université Paris Descartes, École Nationale Supérieure de Chimie de Paris − Chimie ParisTech, UMR 8151 CNRS and U 1022 INSERM, 11 rue Pierre et Marie Curie, 75005 Paris, France

[⊥]Laboratoire de Cristallographie et Modélisation Moléculaire du Solide, Sanofi-Aventis LGCR, 371 rue du Professeur Blayac, 34184 Montpellier Cedex 04, France

S *Supporting Information*

ABSTRACT: In regard to semirigid donor−spacer−acceptor (D−S−A) dyads devised for photoinduced charge separation and built from an unsaturated spacer, there exists a strategy of design referred to as "geometrical decoupling" that consists in introducing an inner-S twist angle approaching 90° to minimize adverse D/A mutual electronic influence. The present work aims at gaining further insights into the actual impact of the use of bulky substituents (R) of the alkyl type on the electronic structure of spacers (S) of the oligo-*p*-phenylene type, which can be critical in the functioning of derived dyads. To this end, a series of 12 novel expanded pyridiniums (EPs), regarded as model S−A assemblies, was synthesized and its

structural, electronic, and photophysical properties were investigated at both experimental and theoretical levels. These EPs result from the combination of 4 types of pyridinium-based acceptor moieties with the three following types of S subunits connected at position 4 of the pyridinum core: xylyl (X), xylyl-phenyl (XP), and xylyl-tolyl (XT). From comparison of collected data with those already reported for eight other EPs based on the same A components but linked to S fragments of two other types (i.e., phenyl, P, and biphenyl, PP), the following quantitative order in regard to the pivotal S-centered HOMO energy perturbation was derived (sorted by increasing destabilization): P < X ≪ PP ≈< XP ≈< XT. This indicates that spacers (S) are primarily distinguished on the basis of their mono- or biaryl composition and secondarily by their number of methyl substituents (R). The electron-donating inductive contribution of methyl substituents (HOMO destabilization) more than counterbalances the effect of conjugation disruption (HOMO stabilization). This "compensation effect" suggests that mildly electron-withdrawing hindering groups are better suited for "geometrical decoupling", given that high-energy S-centered occupied MOs can assist charge recombination within D−S−A dyads.
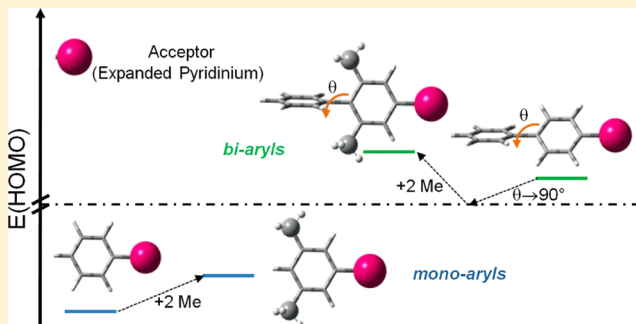
1. INTRODUCTION

In the field of artificial photosynthesis, a wealth of work is devoted to the design of (supra-)molecular assemblies that efficiently convert the energy of light to electrochemical energy. The function of these photochemical molecular devices (PMDs)[1] is to achieve photoinduced charge separation, which constitutes one of the key steps of natural photosynthesis. Simplest models of such transducers are made up of a photosensitizer, which generally behaves as a light-triggered primary electron donor (D) and of an electron-accepting unit (A). D and A components are covalently linked via a spacer (S) to form the D−S−A dyad transducer.[2] Originally, S was

supposed to be a passive element of the functional architectures that primarily holds the structural role of gathering together the D/A "active" partners (while preserving their electronic integrity) in view to circumvent the effects of diffusion present in solution. Over the years, as the level of tuning of these PMDs has become more acute, S was progressively assigned to serve as a connector that facilitates intramolecular electron transfer (ET) by transmitting intercomponent communication (namely, energy gradient) via a little intramolecular electronic coupling. In recent years, electronically closely coupled PMDs have naturally emerged whereby S takes a full "active" part in photoinduced processes, thereby offering the opportunity to explore the limits of multifunctional integration at the molecular level: when the behavior of the assembly switches from that of a supramolecular species (made up of electronically identifiable components) to that of a mere "large molecule" worth considered as electronically made-in-one-piece.[3−5]

In fact, one can trace back the evolution of the role of S in the 2-fold quest of chemists for (1) exerting an ever more precise control over the spatial layout of PMDs' elementary components, which correlates with a propensity to rigidifying functional assemblies, and (2) optimizing the energetic efficiency of PMDs, which not only includes improved chromophoric activity of D within the solar energy spectral range but also the proper matching of the relevant frontier molecular orbitals (MOs) of photoexcited D−S−A assemblies (e.g., HOMO/LUMO) with relevant energy levels of components ensuring the subsequent transduction step.[6] Thus, from the viewpoint of molecular design, strictly meeting the requirements of fine-tuning, especially for the structural aspect, most often entails demanding synthetic efforts unless tolerating a non-negligible intercomponent electronic coupling. Typically, rather than exploiting the appealing features of insulating (saturated), rod-like, and rigid adamantane, bicyclooctane, or stellane fragments as spacers,[7] for instance, it is more convenient to implement unsaturated fragments such as aryl, ethylenyl, ethynyl, and their combinations. In so doing, however, not only is the gain in rigidity obtained at the expense of a sizable intramolecular electronic coupling (as compared to flexible but insulating oligo-methylene fragments, for instance), but also potentially polarizable π-systems, are introduced that can give rise to more or less pronounced intramolecular charge-transfer (ICT) processes. In other words, upon direct connection of an unsaturated S fragment to A (and even D), the S−A (or D−S−A) assembly acquires a certain chromophoric activity (charge transfer character) that can affect the functioning of the molecular transducers, in particular, with respect to photoinduced ET for charge separation. As far as possible, it is therefore of utmost importance to control both the intramolecular electronic coupling and the ancillary (i.e., extra D) chromophoric activity introduced by unsaturated S in view to turning them into good account, that is, to take advantage of them.

In this regard, the most widely adopted strategy relies on the so-called "geometrical decoupling" of D/A components within the potentially fully conjugated D−S−A semirigid assembly.[3,4,8−10] This is therefore one of the functions operated by the spacer S. The precise relative positioning in space of D/A subunits is not only defined in terms of distance but also with respect to angular parameters (e.g., θ_S or θ_D/θ_A; Chart 1). Thus, the intervening tilt angle (θ) that approaches 90° is first aimed at reducing drawbacks of too strong intramolecular

Chart 1. Schematized General Representation of D−S−A Assemblies with Relevant Angular Parameters (Top) along with the Corresponding Basic Molecular Structure and Related Numbering Scheme for the S−A Model Assemblies Herein Studied (Bottom)[a]
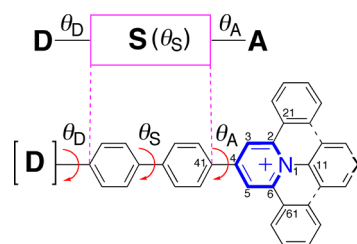

[a] The pyridinium core of the component A is indicated in bold blue. X = N, N+−CH3.

electronic coupling mediated by unsaturated S (in particular, alteration of the electronic integrity of D/A components) and second at decreasing electron transfer rates, in particular, useful when suitably designed to slow down charge recombination. The most convenient way to obtain this geometrical decoupling ($\theta \approx 90°$) usually relies on intramolecular steric hindrance: several bulky substituents are introduced at key locations of S (whether at one of the connection sites to D/A active moieties (θ_D/θ_A)[9a,b] or within the body of S (θ_S)). The fact remains that twisted π-systems bridging electron-donor and -acceptor moieties are still known to exhibit ICT character and to behave as so-called TICTOID chromophores.[11] Besides, the hindering groups are usually of the alkyl (e.g., methyl) or alkoxy (e.g., methoxy) types,[12] and the question can be raised of the actual magnitude of their electronic impact on the electronic structure of S and beyond, that is, on that of D−S−A assemblies. The goal of the present study is to assess this issue.

In the continuation of our work devoted to photoinduced charge separation within semirigid inorganic dyads based on Ru(II)/Os(II) polypyridine complexes (as the D component) with appended pyridinium derivatives (as the A component), we will naturally rely on the prototypical pyridinium for the modeling of S−A subsystems (i.e., D−S−A assemblies deprived of the strongly chromophoric and photoactive D unit). In a series of recent studies,[13−16] we demonstrated how the redox, electronic, and photophysical properties of pyridinium derivatives (referred to as expanded pyridiniums, EPs) can be rationally improved by ad-hoc functionalization of the pyridinium core. Basically, two types of approaches were conceived. On one hand, the π-conjugated system of the pyridinium core was extended by aryl (per)substitution to give *branched* EPs (quoted as B), which subsequently underwent photochemical ring fusion to give *fused* EPs (quoted as F). On the other hand, the synergistic effect resulting from the connection of a second pyridinium at the N-pyridinio site of the pyridinium core to give *head-to-tail* bipyridiniums (of both B and F types) was exploited. This work led to the synthesis and characterization of a series of EPs whose most promising representatives as electron acceptors for D−S−A inorganic dyads, are represented in Chart 2.

In this contribution, we assess the impact of the use of methyl substituents as hindering groups to produce intraspacer geometrical decoupling (i.e., θ_S in Chart 1) in the simple case of a biphenylene spacer. Both the number of methyl substituents (n = 0, 2, 3) and the number of (substituted) phenylene subunits (m = 1, 2) were varied systematically, affording the

Chart 2. Molecular Structures along with Related Labels of the S−A Assemblies, Based on Branched and Fused EPs[a]
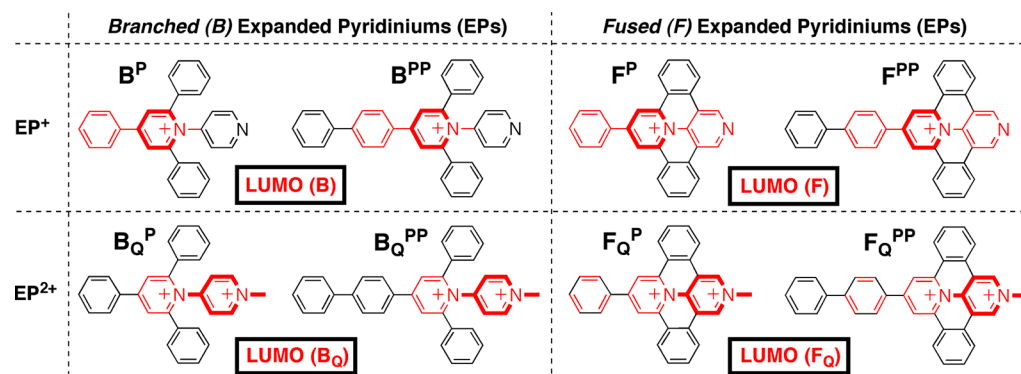
[a]Studied in ref 15 nomenclature: subscript Q refers to quaternized (dicationic) species while superscripts P and PP indicate that S is comprised of 1 or 2 phenyl subunits, respectively. The spatial expanse of four reference LUMOs (quoted as B, B_Q, F, and F_Q) is indicated in red (bold: main location); see text and ref 15.

**Chart 3. Molecular Structures along with Related Labels of the S−A Assemblies Herein Studied[a]**
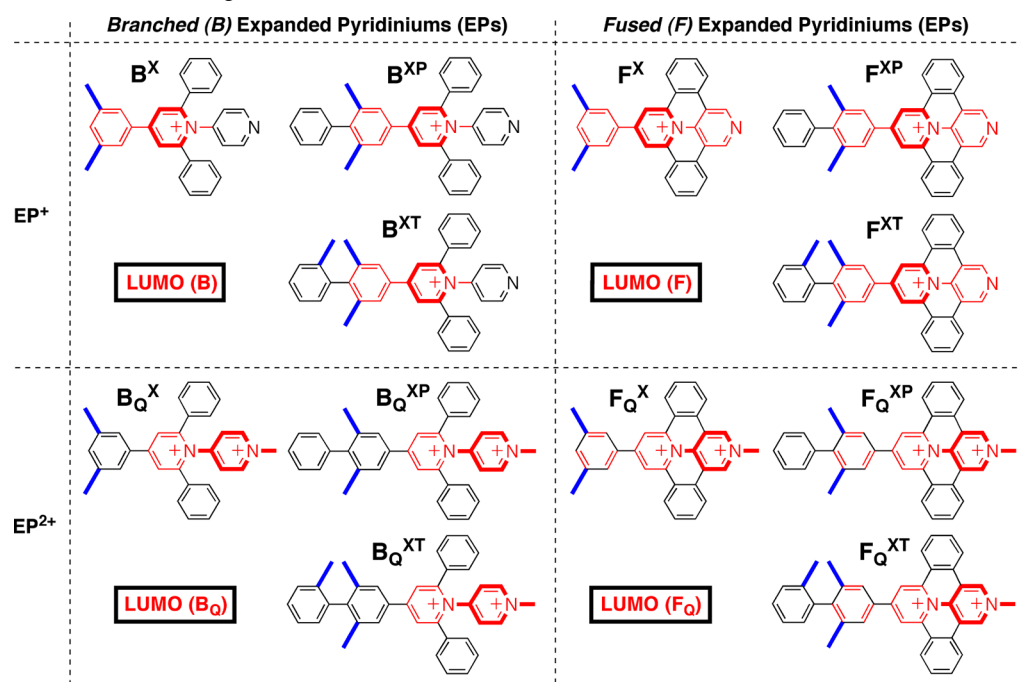
[a]Nomenclature: superscripts **X**, **T**, and **P** refer to xylyl, tolyl, and phenyl fragments of S, respectively. The spatial expanse of four reference LUMOs (quoted as **B**, B_Q, **F**, and F_Q) is indicated in red (bold: main location); see text.

series of 12 new S−A model assemblies depicted in Chart 3, which were synthesized and fully characterized. To disentangle the anticipated conflicting contributions of structural and electronic effects related to the presence of methyl substituents, experimental investigations have been completed by a theoretical study of the structural and electronic features of prominent representatives of the two families of compounds (B and F). To this end, density functional theory (DFT)[17] and time-dependent DFT (TD-DFT)[18] were applied to fully characterize their ground and excited states.

Nowadays, a combined use of DFT and TD-DFT has become a reliable and extensively benchmarked tool for analysis and prediction of ground state properties as well as of vertical absorption spectra of organic chromophores.[19,20] In particular, the computational protocol here applied is able to provide valence excitations of organic dyes with an average error of a

few tenths of eV,[21] if solvent effects are also properly taken into account. A similar computational protocol has been validated in the case of emission energies.[14]

The paper is organized as follows. After discussion of the synthetic strategies along with structural and redox features (section 2.1), absorption (section 2.2), and emission (section 2.3), properties of both fused (F) and branched (B) architectures will be analyzed. By the discussion of experimental and theoretical results, some insights of general interest on the effects induced at both structural and electronic levels by the use of methyl substituents will be drawn. Finally, some perspectives on future work in the design and modeling of pyridinium-based acceptors for PMDs destined to photo-induced charge separation will be given.

Scheme 1. General Synthetic Strategies Developed to Obtain Various Types of S−A Model Systems Shown in Chart 3[a]
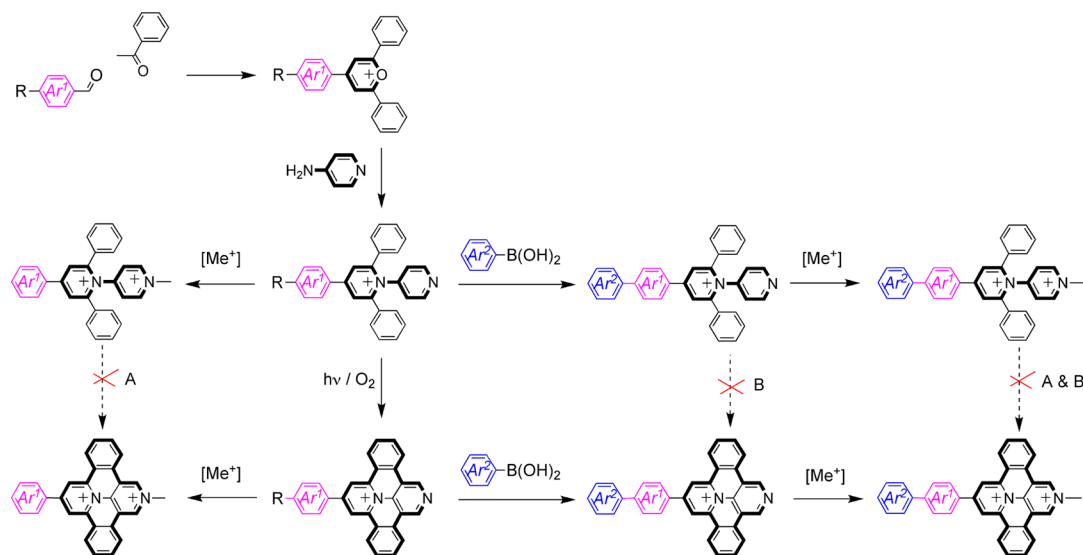
[a]R = H or Br. Routes A and B correspond to inhibited photochemistry. See Supporting Information for details.

2. RESULTS AND DISCUSSION

2.1. Syntheses and Structural Characterization.

2.1.1. Synthesis. The general synthetic strategy to obtain various S−A model compounds (Chart 3) is given in Scheme 1. Pericondensation of the proper branched EPs to obtain their fused derivatives has been performed photochemically, following a route adapted[13,15,22] from that first described by Katritzky and co-workers three decades ago.[23] The overall strategy (Scheme 1) was conceived to circumvent two previously identified obstacles related to a lack of photoreactivity, namely, quaternization (route A) and the presence of a biphenylene S fragment (route B) that both inhibit photobiscyclization.[14,15]

2.1.2. Structural Characterization. To evaluate the structural decoupling produced by the presence of intraspacer methyl groups, X-ray structures of $\mathbf{B^{PP}}$ and $\mathbf{F_Q^{XT}}$ species were solved (see Experimental Section).[24] ORTEP drawings of molecular entities and selected structural parameters are collected in Figure 1 and Table 1, respectively.

First, as regards the structural features of the pyridinium core, it is worth noting that no noticeable bond-length equalization is observed in going from branched to fused EPs (represented by $\mathbf{B^{PP}}$ and $\mathbf{F_Q^{XT}}$, respectively) that could be related to the effect of the extended π-delocalized system present in pericondensed species. This finding is consistent with both the known prevailing pattern of the pyridinium motif (even when embedded within a fused polycyclic skeleton) and the localized nature of its LUMO (see also the section below dealing with electrochemistry).[13−15]

Second, inspection of structural data (Table 1) reveals that $\mathbf{B^{PP}}$ shows a non-negligible intraspacer (θ_S) twist angle even though this S lacks methyl substituents. This onset of geometrical decoupling is due to the steric repulsion between the H atoms present about the interannular linkage of the two phenyl rings. Most importantly, the X-ray analysis of $\mathbf{F_Q^{XT}}$ indicates that a spacer S built from a tolyl and a xylyl moieties (S = XT) exhibits a virtually "ideal" geometrical decoupling, with a θ_S of 89.32°. Therefore, substitution of a biphenylene bridge with $n = 3$ vicinal methyl groups is sufficient to produce a perfect π−π-conjugation disruption, which avoids embarking

(a)

(b)

(c)
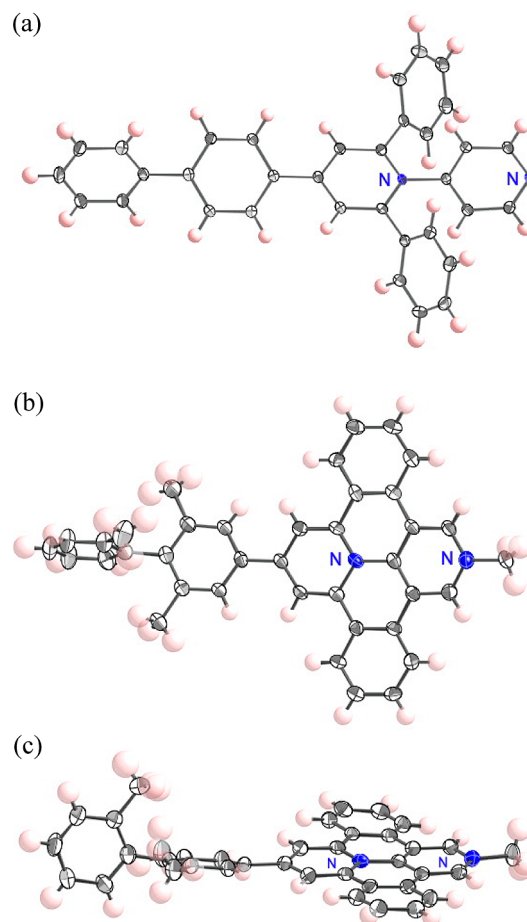
Figure 1. (a) ORTEP drawing of $\mathbf{B^{PP}}(\mathrm{BF_4})$ of one of the two independent molecular entities present in asymmetric unit cell, with thermal ellipsoids (50% probability); the $\mathrm{BF_4^-}$ counteranion and cocrystallized acetone and water solvent molecules have been omitted for clarity. (b and c) ORTEP drawings (top and side views) of $\mathbf{F_Q^{XT}}(\mathrm{PF_6})_2$ model S−A with thermal ellipsoids (50% probability); the two $\mathrm{PF_6^-}$ counter-anions have been omitted for clarity.

Table 1. Selected X-ray Structural Parameters about the Pyridinium Core of A and along the Main Molecular Axis of S−A Species[a]

	$B^{PP b}$	F_Q^{XT}
N_1-C_2	1.370/1.367	1.418
N_1-C_6	1.371/1.363	1.378
C_2-C_3	1.374/1.378	1.371
C_5-C_6	1.379/1.379	1.377
C_3-C_4	1.398/1.385	1.402
C_4-C_5	1.394/1.389	1.357
C_2-C_{21}	1.486/1.489	1.450
C_4-C_{41}	1.475/1.480	1.495
C_6-C_{61}	1.482/1.483	1.473
θ_A	29.35/46.79	15.62
θ_S	49.41/23.31	89.32

[a]Bond lengths in Å and angles between mean planes in degrees. See Chart 1 for numbering scheme and angular labels. [b]The two given values for each parameter correspond to the two independent molecules found in the asymmetric unit cell (see Experimental Section).

in synthetically more demanding xylyl−xylyl derivatives. From this viewpoint, the semirigid and rodlike tolyl−xylyl unit fulfills the requirements of an ideal spacer for D−S−A dyads designed to undergo photoinduced charge separation since it would enable to fully decouple (that is, orthogonalize) the photosensitizer from the acceptor (EP-based) unit.

2.1.3. Redox Behavior. To get insights into correlations between structural characteristics of S−A assemblies and energy variations of their frontier MOs, electrochemical investigations were undertaken. Collected data are gathered in Table 2. As expected, no redox activity was recorded in the oxidation regime in the potential range relevant for D−S−A assemblies comprised of a Ru(II)/Os(II)−polypyridine complex as the D component, that is, up to +1.5 V versus SCE in acetonitrile (MeCN).[3]

Table 2. Electrochemical Data and Assignment of the First Two Reduction Processes for Examined S−A Assemblies in MeCN + 0.1 M TBAPF$_6$ at Pt Electrode[a]

S−A assembly	LUMO type[b]	$A^{Z/(Z-1)}/A^{Z/(Z-2)}$ $E_{1/2}$	n	$A^{(Z-1)/(Z-2)}$ $E_{1/2}$	n
B^X	B	−0.94	2		
B^{XP}	B	−0.93	2		
B^{XT}	B	−0.94	2		
B_Q^X	B_Q	−0.63	2		
B_Q^{XP}	B_Q	−0.60	2		
B_Q^{XT}	B_Q	−0.62	2		
F^X	F	−0.85	1	−1.64[c]	1
F^{XP}	F	−0.85	1	−1.64[c]	1
F^{XT}	F	−0.86	1	−1.64	1
F_Q^X	F_Q	−0.43	1	−1.09	1
F_Q^{XP}	F_Q	−0.43	1	−1.08	1
F_Q^{XT}	F_Q	−0.44	1	−1.09	1

[a]$A^{Z/(Z-1)}$ and $A^{(Z-1)/(Z-2)}$ refer to one-electron reductions of acceptors of charge Z (case of fused derivatives) while $A^{Z/(Z-2)}$ refers to the two-electron reduction of branched acceptors. $E_{1/2}$/V (vs SCE) is calculated as $(E_{pa} + E_{pc})/2$, where E_{pa} and E_{pc} are the anodic and cathodic peak potentials measured by cyclic voltammetry at 0.1 V s^{-1}; n is the number of electrons involved in the redox process.[15,16] [b]See Chart 3. [c]Square-wave measurement.

Four types of LUMOs (Chart 3) are revealed by reduction properties (Table 2), which differentiate on the bases of both the branched (**B**) or fused (**F**) nature of the acceptor and its native (**B/F**) or quaternized (**B$_Q$/F$_Q$**) nature. As regards each type of LUMO, it is worth noting that neither the presence of methyl groups (n) within the spacer nor the number of spacer aryl subunits ($m = 1$ or 2), has significant energy impact. These findings are consistent with LUMOs essentially located on the A components.

2.2. Absorption Spectra. Experimental absorption spectra of branched and fused species are given in Figure 2.
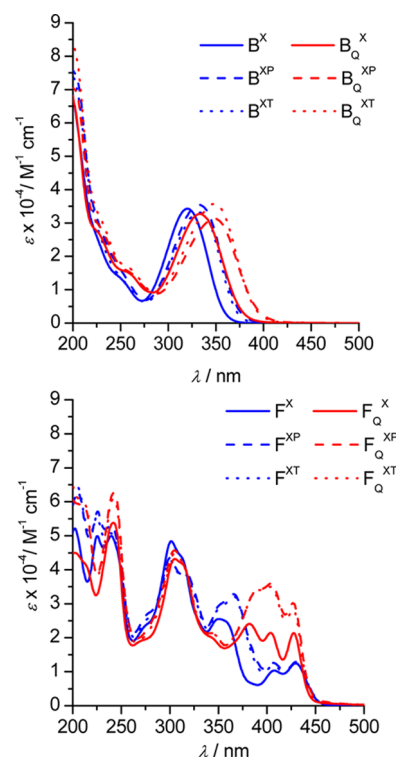
Figure 2. Electronic spectra of branched, **B** (left), and fused, **F** (right), derivatives (MeCN solutions).

2.2.1. Case of the B Series. In MeCN solutions, the spectra of the branched compounds are dominated by a single broad band in the 300−350 nm region. A bathochromic shift of this main absorption band is observed in going from the monopyridiniums (**B** series) to their quaternized, bipyridinium, derivatives (**B$_Q$** series) for a given S moiety, indicating that the electron acceptor moiety present in the latter systems is stronger than that of the former ones, in accordance with redox properties (see Table 2). This finding also suggests that involved electronic transitions have an ICT character.

Similarly, this absorption band is sizably red-shifted in going from a xylyl to a xylyl−phenyl as the S fragment for a given component A, that is, in passing from **B^X** to **B^{XP}** or from **B$_Q^X$** to **B$_Q^{XP}$**. Moreover, the energy of this band remains practically unchanged when going from a xylyl−phenyl to a xylyl−tolyl substituent as the S fragment (that is, in passing from **B^{XP}** to **B^{XT}** and from **B$_Q^{XP}$** to **B$_Q^{XT}$**).

Under the ICT assumption, these observations suggest that S fragments containing two aryl subunits exhibit a stronger electron-donating character than S fragments made up of a

single aryl subunit, regardless of the number (n) of methyl substituents.

DFT and TD-DFT calculations performed for representative molecules (namely, B^{XP}, B_Q^X, and B_Q^{XP}) fully support this picture. The computed electronic transitions (Figure 3) show
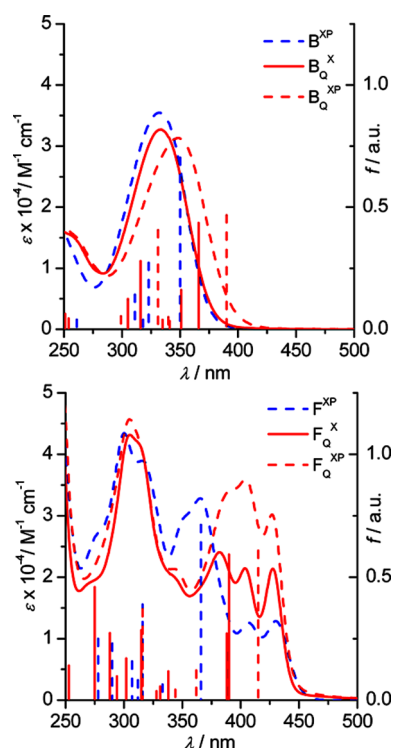

Figure 3. Superimposed computed transitions and experimental electronic spectra of selected branched (left) and fused (right) S—A assemblies (in MeCN). For TD-DFT related data, see Tables S2 and S4 in Supporting Information.

an overall good agreement with the experimental data in spite of systematic energy overestimation, as exemplified by the most intense transitions computed at 350, 366, and 390 nm for B^{XP}, B_Q^X, and B_Q^{XP}, respectively. It is worth noticing that several electronic transitions (two of them more intense and of ICT character) contribute to the experimentally observed absorption band, so that in such a case it is clearly improper to directly compare the experimental λ_{max} to the wavelength corresponding to the sole lowest-energy computed transition. Convoluting the spectra with Gaussian functions (using an empirical full-width at half-maximum parameter of 0.7 eV for each computed transition) leads to a much better agreement between the experimental and the simulated data. The computed λ_{max} values are in such a case 340, 345, and 351 nm for B^{XP}, B_Q^X, and B_Q^{XP}, respectively, in much better agreement with the experimentally observed values of 331, 334, and 348 nm, respectively.

Analyzing the orbitals contributing to the most intense transitions allows confirming that the electronic transitions present in this spectral region essentially originate from intramolecular charge transfers (ICT) involving the electron-releasing aryl substituent at position 4 of the pyridinium core (and, to a lesser extent, also the phenyls at positions 2 and 6; Chart 1),[13-15,25] on one hand, and the electron-withdrawing pyridinium core (**B** series) plus the pyridylium group (**B_Q** series), on the other hand. These transitions essentially correspond to HOMO—LUMO excitations. In Supporting

Information the full list of computed transitions is reported, along with representation of molecular orbitals (MOs).

While it is clear that, overall, a (methyl-substituted)-biphenyl unit is a better electron-donating group than a single (methyl-substituted)-phenyl unit, in line with experimental findings, the electronic role(s) of the methyl substituents —as such— is more difficult to assess.

Analyzing in more detail the HOMO and LUMO energies in the case of the B_Q series, as reported in Figure 4, allows further
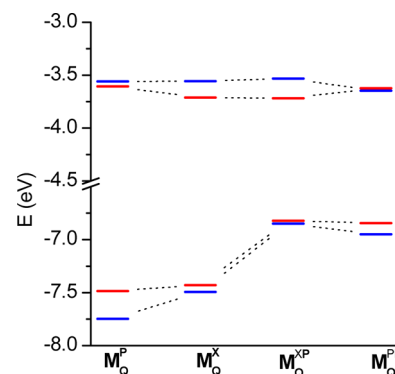

Figure 4. HOMO (bottom) and LUMO (top) energies computed for the B_Q (blue) and F_Q (red) series (**M = B** or **F**).

clarifying the dual, and opposite, roles played by the methyl substituents. Steric hindrance of the methyl substituents produces a structural decoupling within the xylyl—phenyl and xylyl—tolyl S units, which should correlate with an enlarged HOMO—LUMO gap as compared to that of parent biphenyl unit (B_Q^{PP}; Chart 2). Xylyl—phenyl and xylyl—tolyl fragments are therefore anticipated to behave as weaker electron-donating groups than the naked biphenyl group.

In agreement with this qualitative expectation, the dihedral angle computed between the xylyl and phenyl rings (θ_S) within B_Q^{XP} is about 77°, whereas that computed between the two phenyl rings of B_Q^{PP} is only about 31°. One would therefore expect a lowering of the HOMO energy in going from B_Q^{PP} to B_Q^{XP}. However, DFT calculations show that the HOMO energy is roughly the same in B_Q^{PP} and B_Q^{XP} (Figure 4).

This finding is straightforwardly explained by the contribution of the electron-donating inductive effect of methyl substituents. The comparison of the HOMO energies computed for the B_Q^P and B_Q^X systems, which show very similar computed structures except for the presence of the methyl substituents, leads to the observation that the HOMO energy is raised by about 0.25 eV in going from B_Q^P to B_Q^X.

In summary, the effect of the geometrical decoupling produced by the presence of the bulky methyl substituents (namely the intraspacer conjugation disruption with correlated enlarged HOMO—LUMO gap) is more than compensated by the inductive electronic effects of these methyl groups. Accordingly, substituted biphenyl units (xylyl—phenyl or xylyl—tolyl) are globally better electron-releasing groups than a mere substituted phenyl (e.g., xylyl), as experimentally observed,[26] and in agreement with DFT calculations showing that the HOMO energy raises by about 0.8 eV on the average in going from B_Q^X/B_Q^P to B_Q^{XP}/B_Q^{PP}.

On the other hand, the LUMO energy is virtually insensitive to the modifications of the S unit and is only affected by the presence of one or two pyridinium units within the A component, where this LUMO is essentially localized (the

Table 3. Absorption and Luminescence Data

entry	absorption[a]		luminescence,[a] RT			luminescence,[b] 77 K	
	λ_{em}/nm (ε, $M^{-1}cm^{-1}$)		λ_{em}/nm	Φ_{em}	τ/ns	fluorescence; λ_{em}/nm (τ)	phosphorescence; λ_{em}/nm (τ)
B^X	320 (34 300)		495	0.48	3.4	390 (16 ns)	468 (158 ms)
B^{XP}	331 (35 500)		474	0.36	1.6	404 (2.0 ns)	480 (470 ms)
B^{XT}	332 (33 200)		495	0.10	0.9	390 (1.8 ns)	469 (1.6 s)
$B_Q{}^X$	334 (32 700)		545	0.05	0.3	425 (5.7 ns)	474 (170 ms)
$B_Q{}^{XP}$	348 (31 300)		564	0.09	0.6	418 (2.3 ns)	482 (15 ms)
$B_Q{}^{XT}$	349 (35 700)		575	0.05	0.3	411 (5.7 ns)	476 (2.2 s)
F^X	429 (12 500)		465	0.23	3.3	440 (5.5 ns)	502 (2.0 s)
F^{XP}	430 (12 900)		462	0.20	3.2	440 (5.5 ns)	502 (1.8 s)
F^{XT}	430 (12 400)		463	0.17	3.2	440 (5.2 ns)	501 (1.5 s)
$F_Q{}^X$	428 (21 400)		463	0.28	3.1	434 (5.9 ns)	505 (610 ms)
$F_Q{}^{XP}$	427 (30 200)		567	0.22	3.7	436 (4.2 ns)	500 (150 ms)
$F_Q{}^{XT}$	427 (28 300)		565	0.12	3.4	433 (4.8 ns)	498 (470 ms)

[a]In MeCN solution; the main absorption band (**B** species) or the lowest-energy feature (**F** species) is reported. [b]In MeOH/EtOH 4:1 (v/v) rigid matrix.

LUMO energy is lowered by about 0.5−0.6 eV in going from **B** to **B**$_Q$ types of S−A systems).[27]

2.2.2. Case of the F Series. The fused S−A systems exhibit much more complex absorption spectra than their corresponding branched counterparts (Figure 2). Analogously to their parent fused compounds (Chart 2),[14,15] the spectra are more structured and red-shifted. The structured bands can be simply justified considering that fused species have more rigid structures than the corresponding branched pyridiniums. In addition, a pronounced vibronic progression is also evident for the lowest energy band, similar to the behavior of parent compounds.[28]

TD-DFT calculations, reported in Figure 3, performed for representative molecules (namely, **F**^{XP}, **F**$_Q{}^X$, and **F**$_Q{}^{XP}$) show an overall good agreement with the experimental data. An analysis of the orbitals contributing to the most intense lowest energy transitions allows confirming their (I)CT character, in close analogy to what was found for the branched counterparts. Nonetheless, depending on the nature of the substituents at position 4 of the pyridinium core (Chart 1), the $\pi−\pi^*$ electronic states centered on the fused polycyclic system are found more or less (very) close in energy to the ICT singlet (practically degenerate in the case of **F**$_Q{}^X$). In Supporting Information are reported the full lists of computed transitions along with representation of the orbitals contributing to the most intense transitions.

An analysis of the DFT results shows a densification of MOs close to the HOMO−LUMO gap for the fused compounds, in agreement with the increasing complexity of their absorption spectra. This HOMO−LUMO gap is globally reduced with respect to that of the branched analogues due to the occurrence of two concomitant phenomena: (1) a slight decrease in LUMO energy because of the enforced coplanar layout of the pyridinium core and its N-pyridyl(ium) group, and (2) a slight increase in the HOMO energy. In line with what was found for the parent compounds (Chart 2),[15] HOMOs are higher in energy for the fused compounds than for the corresponding branched ones as a direct consequence of ring fusion (fused polycyclic backbone).

In the case of the fused architectures, the presence of a substituted biphenyl unit in position 4 does not significantly red-shift the lowest energy band, contrary to what happens in the case of the branched systems. In the case of the **F**$_Q$ series, inspection of the MOs involved in the first electronic transition

confirms its ICT character from a HOMO or HOMO-1 (essentially localized on the biphenyl substituent) to the LUMO centered on the pyridinium unit(s) (Supporting Information). The ICT character accordingly translates into an increase of intensity associated to the first band experimentally observed in going from **F**$_Q{}^X$ to **F**$_Q{}^{XP}$.

To summarize, electro-optical features of branched and fused S−A assemblies are essentially governed by ICT transitions largely involving the S fragment linked at position 4 of the pyridinium core of the A units. If the steric hindrance of methyl substituents structurally decouples the so-decorated biphenyl-based spacer units, the resulting energy lowering of the S-centered HOMOs is largely counterbalanced by the electron-donating inductive effect of these bulky groups. As a consequence, the overall spectral behavior of the S−A model compounds results from a subtle interplay of these concurrent effects.

2.3. Emission Properties. All the compounds exhibit luminescence, both in fluid MeCN solutions at room temperature (RT) and in rigid matrices at 77 K in MeOH/EtOH 4:1 (v/v), as reported in Table 3.

2.3.1. Low-Temperature Emission Behavior (Rigid Matrix). All compounds exhibit two emissions (see Table 3 and Figure 5); because of the emission energies and lifetimes, the higher and lower energy emissions are assigned to fluorescence and phosphorescence, respectively, for all compounds. The excited singlet and triplet states from which fluorescence and phosphorescence originate appear to be separated from one another by similar energies in all compounds, so indicating the same nature of the emitting excited states, except for the spin multiplicity. However, a closer inspection of the emission maxima indicates that for the fused compounds (**F** series) quaternization (that is, moving from the F-type compounds to the **F**$_Q$-type species) as well as the presence of methyl substituents on the (bi)phenylene skeleton have only minor effects on the energy of both singlet and triplet emissive states. For example, the fluorescence maxima of **F**^{X}, **F**^{XP}, **F**^{XT}, **F**$_Q{}^X$, **F**$_Q{}^{XP}$, and **F**$_Q{}^{XT}$ are in the narrow range 433−440 nm, and the phosphorescence maxima of the same compounds vary between 498 and 502 nm (Table 3). Also, considering that compounds **F**$_Q{}^P$ and **F**$_Q{}^{PP}$ (see structures in Chart 2) exhibit similar fluorescence and phosphorescence maxima at 77 K in rigid matrix,[15] it seems that both fluorescence and phosphorescence of the **F** compounds in this matrix (MeOH/EtOH)
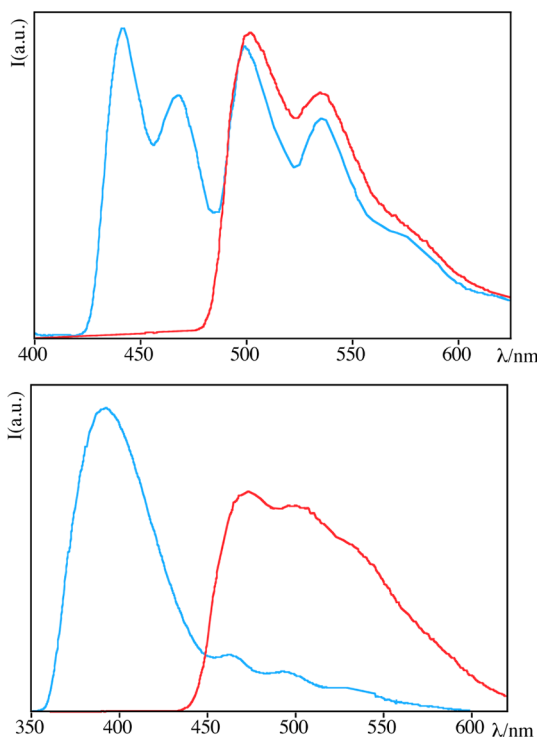
Figure 5. Normalized emission spectra at 77 K of F^{XP} (top) and B^{XT} (bottom) in alcohol matrix. In red are reported the phosphorescence spectra, obtained by using a time delay with respect to the excitation pulse.

originate from excited states that are mainly centered on the fused polycyclic subunit, with only marginal involvement of the (bi)phenyl subunits.

As far as the emission lifetimes are concerned, the phosphorescence lifetimes of the quaternized species F_Q^X, F_Q^{XP}, and F_Q^{XT} are slightly shorter than those of F^X, F^{XP}, and F^{XT} (Table 3), suggesting that quaternization has anyway a sizable effect on the excited state decay at 77 K.

The situation of 77 K emission is different for the **B** series of compounds: for these latter compounds, both fluorescence and phosphorescence maxima are affected by quaternization and by the presence of methyl substituents on the (bi)phenylene backbone. An indication in favor of the net ICT nature of both fluorescence and phosphorescence of the **B**-type compounds is offered by comparison of the emission energies of B^X and B_Q^X with those of the corresponding species lacking methyl S-substituents, that is, B^P and B_Q^P, respectively (see Chart 2): the 77 K fluorescence maxima of the former species are situated at 390 and 425 nm, respectively (Table 3), whereas the latter exhibit fluorescence maxima at 381 and 407 nm, respectively.[15] The red shift of the fluorescence of B^X and B_Q^X with respect to fluorescence of B^P and B_Q^P is attributed to the better electron donor properties conferred by methyl substituents to the phenylene donor subunit. Clearly, the difference in fluorescence energy between B^X and B_Q^X is assigned to the different electron acceptor properties of the dicationic bipyridinium group of B_Q^X with respect to the monocationic pyridinium group of B^X. The same trend is also evident when comparing the phosphorescence energies of the compounds (compare the phosphorescence energies of B^X and B_Q^X shown in Table 3, 468 and 474 nm, respectively, with those of B^P and B_Q^P, 447 and 453 nm, respectively[15]).

Because the 77 K emissive excited states of the **B** series of compounds have significant charge-transfer character, it is not surprising that the fluorescence and phosphorescence maxima span larger ranges compared to the **F** series (Table 3). However, because of the multiple (and in a someway opposite) effects that methyl substituents introduce in the systems investigated (that is, structural decoupling with conjugation disruption and inductive effects, previously discussed in the section dealing with electronic absorption), it is not obvious to discuss in detail the emission shifts on moving within the **B** series of compounds. A further information can be inferred from the 77 K lifetimes of the phosphorescence of **B**-type compounds: for both quaternized and nonquaternized species, the **XT** compounds exhibit a much longer triplet state lifetime compared to the **X** and **XP** compounds (for example, the phosphorescence lifetimes of B^X, B^{XP}, and B^{XT} are 158 ms, 470 ms, and 1.6 s, respectively). This result is ascribed to the rigidifying of the structure due to the presence of the bulky methyl substituents on the xylyl–tolyl aromatic system that lock otherwise present torsional motion of phenyl groups, thereby reducing the efficiency of vibrations involved in nonradiative decay.

2.3.2. Room-Temperature Emission Behavior (Fluid Solution). The room temperature emission of compounds of the **B** type can be straightforwardly assigned to charge-transfer states. By inspection of orbitals involved in the two lowest lying vertical excitations, it is clear that the aromatic substituent connected at position 4 of the pyridinium core (that is, (bi)phenylene units) plays the role of main donor in the case of the first excited state while the phenyl substituents at positions 2 and 6 do the same for the second excited state, the acceptor being always the (bi)pyridinium unit.

As a consequence, functionalization of the aromatic substituents in position 4 results in a sizable change in the emission energies. The emission maximum of B^X, for example, is at 495 nm (Table 3), significantly red-shifted as compared to that of the parent B^P species (435 nm[15]), which does not contain methyl substituents. Similarly, the emission maximum of B_Q^X (545 nm) results in red-shifted emission compared to that of the parent species B_Q^P (455 nm[15]). These data are fully consistent with the results of DFT calculations which show for both systems a HOMO centered on the aromatic substituent in position 4 and an increase in the HOMO energy in going from B_Q^P to B_Q^X as shown in Figure 4. The red-shift of the emission on passing from B_Q^P to B_Q^X is attributed to the effect of methyl substitution on the phenyl unit, so further decreasing the energy of the emitting CT state.

Before discussing the room temperature properties of the **F**-type compounds, a final comment is needed for the **B**-type species: there is a very large red-shift for the fluorescence emission on passing from 77 K to room temperature (compare data in Table 3). Although the emission of the **B**-type compounds can be assigned to CT states in both conditions, this suggests that a significant structural reorganization takes place for the emissive excited states of all the **B**-type compounds in fluid solution at room temperature, whereas such a large reorganization could be (at least partially) inhibited in rigid matrix at 77 K. To support this suggestion, Figure 6 shows that the room temperature emission spectra of such compounds are quite broad (half-height width even larger than 4000 cm^{-1}), typical of excited states having a geometry that significantly differs from that of ground states. Similar conclusions have been suggested for the parent B^P-type
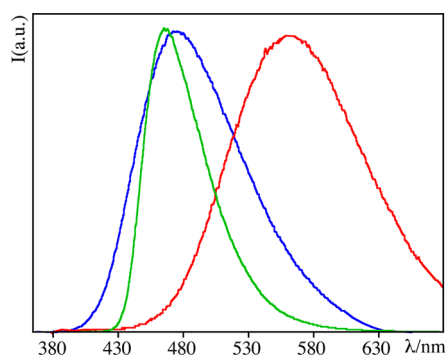
Figure 6. Normalized emission spectra of $\mathbf{B^{XP}}$ (blue curve), $\mathbf{B_Q^{XP}}$ (red curve), and $\mathbf{F^X}$ (green curve) in MeCN at room temperature.

compounds shown in Chart 2.[15] Most likely, the main structural reorganization occurring in the excited states of the **B**-type compounds can include, besides a planarization around θ_A, also some planarization involving the phenyl rings in 2 and 6 positions of the pyridinium central ring.

The room temperature emission of $\mathbf{F^X}$, $\mathbf{F^{XP}}$, $\mathbf{F^{XT}}$, and $\mathbf{F_Q^X}$, whose emission maxima are in the small range between 462 and 465 nm (Table 3, see Figure 6 for the emission spectra of $\mathbf{F^X}$ as a representative compound) can be assigned to singlet states centered on the fused systems, with negligible ICT character. The relatively narrow emission bands of these compounds (see Figure 6, half-height width of the emission band of $\mathbf{F^X}$, about 2500 cm^{-1}) indicates that the emissive states have geometries quite similar to those of the respective ground states, contrary to **B**-type compounds, thus, further substantiating the absence of a significant ICT character.

On the contrary, the emission of $\mathbf{F_Q^{XP}}$ and $\mathbf{F_Q^{XT}}$ seem to have a more pronounced CT nature than the other **F**-type compounds, as indicated by the large red-shift of the emission compared to 77 K emission (Table 3) and the broad emission bands (about 4000 cm^{-1} for $\mathbf{F_Q^{XP}}$, not shown).

Close inspection of the computed molecular orbitals involved in the low lying electronic transitions may help in rationalizing the differences in emission behavior observed between branched and fused analogues, as well as the peculiar behavior of the $\mathbf{F_Q^{XP}}$ and $\mathbf{F_Q^{XT}}$ systems.

In the case of the nonquaternized fused compounds (**F** series), the HOMO is always localized on the fused polycyclic moiety, so that any emissive state corresponding to the HOMO−LUMO excitation (that is, the lowest energy singlet state) is predicted to be of $\pi-\pi^*$ character and for such a state a large structural reorganization is not expected, similar to what is observed for the parent, phenyl-substituted compound **Ref-F** shown in Chart 4.[14]

On the other hand, in the case of quaternized fused compounds (**F$_Q$** series), all compounds show HOMO and HOMO-1 orbitals centered on the aromatic substituent at position 4 (that is, **X**, **XP**, or **XT**, see Supporting Information).

Chart 4. Structural Formula of Reference Compound Ref-F

Ref-F
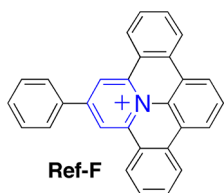
These orbitals contribute to the first electronic transition which is, thus, of ICT character. The $\mathbf{F_Q^X}$ system represents a notable exception, because the above-mentioned HOMO and HOMO-1 orbitals are practically degenerate with an occupied orbital (the HOMO-2) centered on the fused polycyclic system (Figure 7). This latter orbital is involved in a $\pi-\pi^*$ electronic
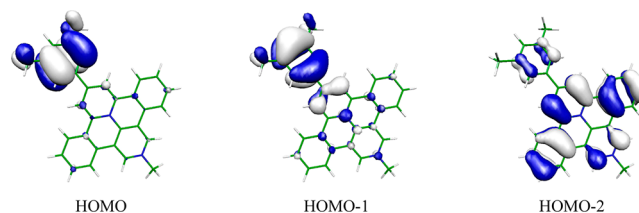

HOMO   HOMO-1   HOMO-2

Figure 7. Isocontour representation of the highest occupied MOs computed for $\mathbf{F_Q^X}$.

transition computed to be (in absorption) practically isoenergetic to the above-mentioned ICT state (390 vs 388 nm computed for the ICT and $\pi-\pi^*$ transitions, respectively, see Supporting Information). On the basis of such an orbital configuration, while $\mathbf{F_Q^{XP}}$ and $\mathbf{F_Q^{XT}}$ will give rise to net CT emissive states, emission for $\mathbf{F_Q^X}$ will take place from the $\pi-\pi^*$ singlet state, thus, giving rise to energies very similar to the **F** series, in perfect agreement with the experimental observations.

3. SUMMARY AND CONCLUDING REMARKS

In the case of semirigid donor−spacer−acceptor (D−S−A) dyads designed for photoinduced charge separation and built from an unsaturated S of oligo-p-phenylene type, the HOMO and LUMO are normally located at the photosensitizing unit (D) and at the electron-accepting component (A), respectively. As regards the electronic structure typical of derived spacer−acceptor (S−A) model assemblies, the HOMO is in this case localized on the S moiety, while the LUMO remains essentially localized on the A subsystem. With this difference in mind, the picture of the HOMO energy variation drawn out of the present study of the present series of 12 expanded pyridiniums (EPs) as S−A models can therefore be transposed to D−S−A dyads, with the caveat that higher lying occupied MOs centered on S must then be considered instead.

By combining experimental and computational approaches, we have investigated the electronic structure of these tictoid EPs to assess the impact of the design strategy referred to as "geometrical decoupling", which relies on the use of steric hindrance produced by alkyl substituents (here, methyl groups) about the interannular linkage inner to a biphenyl-based S for minimizing the adverse mutual electronic influence of D and A active components. More precisely, the variation of their HOMO−LUMO energy gap has been more specifically investigated. We have shown that the old fashion discussion based upon the relative contributions of conjugation (i.e., mesomeric or resonance effects) and through-bond inductive effect, remains qualitatively relevant in the present case study. Indeed, provided that the S-centered HOMO is primarily affected because the LUMO is essentially localized on A, we found that the enlarged HOMO−LUMO gap that normally results from intra-S conjugation disruption due to geometrical decoupling (following the energy stabilization of the HOMO) is more than counterbalanced by the energy destabilization of this HOMO originating from electron-releasing inductive effect

of alkyl substituents used for the conformational change. We refer to this phenomenon as the "compensation effect".

The present work gathers information gained for the 12 new EPs, which result from the combination of four types of pyridinium-based electron-acceptor moieties A (and the corresponding four types of LUMOs denoted **B**, **B$_Q$**, **F**, and **F$_Q$**; Chart 3) and three types of spacer models S (that is, xylyl, xylyl—phenyl, and xylyl—tolyl moieties denoted as **X**, **XP**, and **XT**, respectively; Chart 3), along with previously reported data[15] for eight other EPs based on the same A components (**B**, **B$_Q$**, **F**, and **F$_Q$**; Chart 2) but linked to S fragments of two other types (i.e., bare phenyl and biphenyl moieties, denoted as **P** and **PP**, respectively; Chart 2). From the comparison of data collected for this library of 20 S—A model species, we derived the following quantitative order as regards the S-centered HOMO energy perturbation (sorted by increasing destabilization): $P < X \ll PP \lesssim XP \lesssim XT$. In other words, spacers (S) are primarily distinguished on the basis of their mono- or biaryl composition and secondarily by the number of methyl substituents they carry. Further experimental and theoretical work using different electron-withdrawing groups could be undertaken to generalize these findings.

Given that higher-lying occupied MOs of S within D—S—A dyads can play a critical role in charge recombination by assisting hole transfer,[12,29] thereby shortening accordingly the lifetime of charge-separated states, the above-mentioned "compensation effect" must be taken into account in the process of molecular design. In no way does this finding bring into question the relevance of the "geometrical decoupling" strategy, but this suggests the use of electron-withdrawing rather than electron-releasing groups as bulky substituents. Besides, the electron-withdrawing strength of these hindering group must be properly adjusted (i.e., it should be rather mild) to avoid the undesirable displacement (or extension) of the LUMO on the spacer S, because this LUMO is required to remain centered on the A subunit to form efficiently the targeted D^+—S—A^- photoinduced charge-separated state.

4. EXPERIMENTAL SECTION

4.1. Syntheses, Characterization, and General Experimental Details. Materials and syntheses of the EPs, along with full characterizations, are provided in Supporting Information.

4.2. X-ray Crystal Structure Determination. Intensities were collected on a Bruker-Nonius Kappa CCD diffractometer (Mo Kα, λ = 0.71069 Å, graphite-monochromator), with sample-to-detector distances of 40 mm. The frames were integrated and corrected for Lorentz and polarization effects using DENZO,[30] the scaling and refinements of crystal parameters were performed by SCALEPACK.[30] The structures were solved by direct methods and refined on F^2 with SHELXTL.[31] Non-hydrogen were refined anisotropically, H atoms were refined isotropically using a riding model. CCDC-876848 ([**B^{PP}**(BF$_4$)]) and −876849 ([**F$_Q$^{XT}**(PF$_6$)$_2$]) contain the supplementary crystallographic data for this paper. These data can be obtained free of charge from The Cambridge Crystallographic Data Centre via www.ccdc.cam.ac.uk/data_request/cif.

*Crystal Data for [**B^{PP}**(BF$_4$)].* 2[(C$_{34}$H$_{25}$N$_2$)$^+$,(BF$_4$)$^-$]·2·(C$_3$H$_6$O)·(H$_2$O), M = 1230.92, monoclinic, $P2_1/n$, a = 14.651(3), b = 15.895(3), c = 27.762(6) Å, α = 90, β = 101.73(3), γ = 90°, V = 6330.1(2) Å^3, Z = 4, r_{calc} = 1.292 g·cm^{-3}, m = 0.09 mm^{-1}, T = 123 K, 78261 measured, 17252

independent, 13001 observed reflections (θ < 29.6°), R1 [$I > 2\sigma(I)$] = 0.0606, wR2 (all data) = 0.1888, S = 1.52 for 836 parameters and 683 restraints, residual electron density +0.78/−0.65 eÅ^{-3}. The crystal growth was performed in acetone; the asymmetric unit contains two monocationic ligands associated to their respective counterions, two acetone solvates and one water molecule. One 2-fold orientational disorder was resolved for one BF$_4$ anion; the populations being refined to a 4/1 ratio. Geometry and isotropic parameters (SADI, ISOR) restraints were applied to the BF$_4$ anions and atomic displacement parameters (SIMU) restraints were applied to all species (σ = 0.04). Hydrogen atoms of the water molecule were located in difference Fourier maps.

*Crystal Data for [**F$_Q$^{XT}**(PF$_6$)$_2$].* [(C$_{38}$H$_{30}$N$_2$)$^{2+}$,2(PF$_6$)$^-$], M = 804.58, triclinic, P1 bar, a = 7.925(2), b = 16.055(3), c = 17.098(3) Å, α = 114.32(3), β = 100.04(3), γ = 96.16(3)°, V = 1912.7(2) Å^3, Z = 2, r_{calc} = 1.397 g·cm^{-3}, m = 0.20 mm^{-1}, T = 293 K, 19964 measured, 4534 independent, 2667 observed reflections (θ < 22.1°), R1 [$I > 2\sigma(I)$] = 0.0925, wR2 (all data) = 0.2593, S = 1.48 for 535 parameters and 643 restraints, residual electron density +0.58/−0.30 eÅ^{-3}. The crystal growth was performed in MeCN; only a few tiny needles could be grown, resulting in a severe lack of observed data at high resolution. The asymmetric unit contains one dicationic ligand and two counterions. An axial 2-fold orientational disorder was resolved for one PF$_6$ anion; the populations of the disordered fluorine atoms were refined using SUMP restraints. Similarity of geometry (SADI) and displacement (SIMU) parameters restraints, were applied to all species (σ = 0.03).

4.3. Electrochemical Measurements. Electrochemical experiments were carried out with a conventional three-electrode cell and a PC-controlled potentiostat/galvanostat (Princeton Applied Research Inc., model 263A). The working electrode was a platinum electrode from Radiometer-Tacussel (area, 0.0314 cm^2; diameter, 2.0 mm) mounted in Teflon. Before each experiment, it was carefully polished with 3 and 0.3 μm alumina pastes followed by extensive rinsing with ultrapure Milli-Q water. Platinum wire was used as the counter-electrode and a saturated calomel electrode (SCE) as the reference. Electrolytic solutions, MeCN (Aldrich, anhydrous, 99.8%) containing 0.1 M tetrabutylammonium hexafluorophosphate (TBAPF$_6$, Aldrich, +99%) as supporting electrolyte, were routinely deoxygenated by argon bubbling. The electrochemical properties were determined using a monomer concentration of about 5 mM. All potential values are given versus SCE. The reported numerical values (Table 2) were corrected by using a dissolved Fc$^+$/Fc couple as an internal reference and by setting $E_{1/2}$ (Fc$^+$/Fc) equal to +0.380 V versus SCE in MeCN.[32] Cyclic voltammetry experiments were conducted at a scan rate of 0.1 V·s^{-1}. Square-wave voltammetry experiments were performed with potential sweep rate of 100 mV s^{-1} (pulse height, 25 mV; step height, 10 mV; frequency, 50 Hz).

4.4. Photophysical Properties. For steady-state luminescence measurements, a Jobin Yvon-Spex Fluoromax P spectrofluorimeter was used, equipped with a Hamamatsu R3896 photomultiplier, and the spectra were corrected for photomultiplier response using a program purchased with the fluorimeter. To record phosphorescence spectra at 77 K, a time delay with respect to excitation pulse (1 μs) was applied. The same equipment was used to measure luminescence lifetimes in the ms time scale. For the luminescence lifetimes in the ns time scale, an Edinburgh OB 900 time-correlated single-photon-counting spectrometer was used. As excitation sources, a

Hamamatsu PLP 2 laser diode (59 ps pulse width at 408 nm) and the nitrogen discharge (pulse width, 2 ns at 337 nm) or PicoQuant PDL 800-B laser diode (pulse width, 30 ps at 308 nm) were employed. When necessary, emission decays were deconvoluted by a software purchased from Edinburgh. Emission quantum yields for argon-degassed MeCN solutions of the organic species were determined by using the optically diluted method[33] with anthracene in air-equilibrated ethanol solution (Φ_{em} = 0.2) as quantum yield standard.[34] Experimental uncertainties are as follows: absorption maxima, 1 nm; emission maxima, 4 nm; molar absorption values, 10%; luminescence lifetimes, 10%; luminescence quantum yields, 15%.

4.5. Computational Methods. All calculations were carried out at DFT level using the Gaussian code.[35] Unless otherwise specified, a hybrid Hartree−Fock/Density Functional model, referred to as PBE0, was used.[36] For the structural optimizations and the calculation of the electronic properties, all atoms were described by a double ζ quality basis set.[37] The molecular structure of each compound was fully optimized. Optical transitions were computed using the time-dependent DFT approach at the same level of theory. For clarity, only computed transitions with non-negligible oscillator strength are reported in the tables. In this paper only singlet−singlet (i.e., spin-allowed) transitions are discussed. The transitions were computed at least down to 200 nm for all the systems studied. The polarizable continuum model (PCM) of Tomasi and co-workers[38] was applied as implicit solvation model to simulate solvent effects. More specifically, we used the conductor-like PCM model, as implemented in Gaussian code (CPCM). Acetonitrile was considered as solvent.

ASSOCIATED CONTENT

S Supporting Information

Complete reference 35. Main computed structural and electronic (absorption energies and orbitals representations) features. Experimental details regarding the syntheses and characterizations of new compounds and precursors, including ^{1}H NMR (500 MHz) and ^{13}C NMR (126 MHz) spectra, as well as ESI-mass spectra; a summary of the crystallographic data for $[\mathbf{F_Q}^{PP}(PF_6)_2]$ (PDF). X-ray structural data for $[\mathbf{B}^{PP}(BF_4)]$ and $[\mathbf{F_Q}^{XT}(PF_6)_2]$ (CIF). This material is available free of charge via the Internet at http://pubs.acs.org.

AUTHOR INFORMATION

Corresponding Author

*E-mail: philippe.laine@univ-paris-diderot.fr; ilaria-ciofini@ chimie-paristech.fr; campagna@unime.it.

Notes

The authors declare no competing financial interest.

ACKNOWLEDGMENTS

REFERENCES

(1) Ceroni, P.; Credi, A.; Venturi, M.; Balzani, V. *Photochem. Photobiol. Sci.* **2010**, *9*, 1561−1573.

(2) Balzani, V.; Credi, A.; Venturi, M. *ChemSusChem* **2008**, *1*, 26−58.

(3) Lainé, P. P.; Campagna, S.; Loiseau, F. *Coord. Chem. Rev.* **2008**, *252*, 2552−2571.

(4) Lainé, P. P.; Ciofini, I.; Ochsenbein, P.; Amouyal, E.; Adamo, C.; Bedioui, F. *Chem.—Eur. J.* **2005**, *11*, 3711−3727.

(5) Ciofini, I.; Adamo, C.; Teki, Y.; Tuyèras, F.; Lainé, P. P. *Chem.—Eur. J.* **2008**, *14*, 11385−11405.

(6) Typically, the standard Gibbs-free energy change for chemical reactions enabled by coupled catalysts must be taken into account when electrochemical-to-chemical transduction is concerned, while edges of valence (VB)/conduction (CB) bands of semiconductors (SC) in (tandem) dye-sensitized solar cells (DSSCs) are to be considered for electricity or electrolytic (e.g., H$_2$) productions.

(7) De Cola, L.; Belser, P.; Von Zelewsky, A.; Vögtle, F. *Inorg. Chim. Acta* **2007**, *360*, 775−784.

(8) (a) Lainé, P.; Bedioui, F.; Ochsenbein, P.; Marvaud, V.; Bonin, M.; Amouyal, E. *J. Am. Chem. Soc.* **2002**, *124*, 1364−1377. (b) Lainé, P.; Bedioui, F.; Amouyal, E.; Albin, V.; Berruyer−Penaud, F. *Chem.—Eur. J.* **2002**, *8*, 3162−3176. (c) Lainé, P.; Amouyal, E. *Chem. Commun.* **1999**, 935−936.

(9) (a) Lainé, P. P.; Bedioui, F.; Loiseau, F.; Chiorboli, C.; Campagna, S. *J. Am. Chem. Soc.* **2006**, *128*, 7510−7521. (b) Lainé, P. P.; Loiseau, F.; Campagna, S.; Ciofini, I.; Adamo, C. *Inorg. Chem.* **2006**, *45*, 5538−5551. (c) Ciofini, I.; Lainé, P. P.; Bedioui, F.; Adamo, C. *J. Am. Chem. Soc.* **2004**, *126*, 10763−10777.

(10) Selected recent references: (a) Meylemans, H. A.; Damrauer, N. H. *Inorg. Chem.* **2009**, *48*, 11161−11175. (b) Hanss, D.; Wenger, O. S. *Eur. J. Inorg. Chem.* **2009**, 3778−3790. (c) Indelli, M. T.; Chiorboli, C.; Flamigni, L.; De Cola, L.; Scandola, F. *Inorg. Chem.* **2007**, *46*, 5630−5641. (d) Benniston, A. C.; Harriman, A.; Li, P.; Patel, P. V.; Sams, C. A. *J. Org. Chem.* **2006**, *71*, 3481−3493. (e) Benniston, A. C.; Harriman, A. *Chem. Soc. Rev.* **2006**, *35*, 169−179.

(11) (a) Kang, H.; Facchetti, A.; Zhu, P.; Jiang, H.; Yang, Y.; Cariati, E.; Righetto, S.; Ugo, R.; Zuccaccia, C.; Macchioni, A.; Stern, C. L.; Liu, Z.; Ho, S.-T.; Marks, T. J. *Angew. Chem., Int. Ed.* **2005**, *44*, 7922−7925. (b) Albert, I. D. L.; Marks, T. J.; Ratner, M. A. *J. Am. Chem. Soc.* **1998**, *120*, 11174−11181.

(12) Walther, M. E.; Wenger, O. S. *ChemPhysChem* **2009**, *10*, 1203−1206.

(13) Fortage, J.; Tuyèras, F.; Ochsenbein, P.; Puntoriero, F.; Nastasi, F.; Campagna, S.; Griveau, S.; Bedioui, F.; Ciofini, I.; Lainé, P. P. *Chem.—Eur. J.* **2010**, *16*, 11047−11063.

(14) Peltier, C.; Adamo, C.; Lainé, P. P.; Campagna, S.; Puntoriero, F.; Ciofini, I. *J. Phys. Chem. A* **2010**, *114*, 8434−8443.

(15) Fortage, J.; Peltier, C.; Nastasi, F.; Puntoriero, F.; Tuyèras, F.; Griveau, S.; Bedioui, F.; Adamo, C.; Ciofini, I.; Campagna, S.; Lainé, P. P. *J. Am. Chem. Soc.* **2010**, *132*, 16700−16713.

(16) Fortage, J.; Peltier, C.; Perruchot, C.; Takemoto, Y.; Teki, Y.; Bedioui, F.; Marvaud, V.; Dupeyre, G.; Pospisil, L.; Adamo, C.; Hromadova, M.; Ciofini, I.; Lainé, P. P. *J. Am. Chem. Soc.* **2012**, *134*, 2691−2705.

(17) (a) Ziegler, T *Chem. Rev.* **1991**, *91*, 651−667. (b) Cramer, C. J.; Truhlar, D. G. *Phys. Chem. Chem. Phys.* **2009**, *11*, 10757−10816.

(18) Burke, K; Werschnik, J; Gross, E. K. U. *J. Chem. Phys.* **2005**, *123*, 062206−2.

(19) Jacquemin, D.; Perpète, E. A.; Ciofini, I.; Adamo, C. *Acc. Chem. Res.* **2009**, *42*, 326−334.

(20) Improta, R. In *Computational Strategies for Spectroscopy: From Small Molecules to NanoSystems*; Barone, V., Ed.;John Wiley & Sons, Inc.: Hoboken, NJ, 2011; pp 39−77.

(21) (a) Le Bahers, T.; Pauporté, T.; Scalmani, G.; Adamo, C.; Ciofini, I. *Phys. Chem. Chem. Phys.* **2009**, *11*, 11276−11284. (b) Le Bahers, T.; Pauporté, T.; Labat, F.; Lainé, P. P.; Ciofini, I. *J. Am. Chem. Soc.* **2011**, *133*, 8005−8013. (c) Rekhis, M.; Labat, F.; Ouamerali, O.; Ciofini, I.; Adamo, C. *J. Phys. Chem. A* **2008**, *111*, 13106−13111.

(22) Di Pietro, M. L.; Puntoriero, F.; Tuyèras, F.; Ochsenbein, P.; Lainé, P. P.; Campagna, S. *Chem. Commun.* **2010**, *46*, 5169−5171.

(23) (a) Katritzky, A. R.; Zakaria, Z.; Lunt, E.; Jones, P. G.; Kennard, O. *J. Chem. Soc., Chem. Commun.* **1979**, 268−269. (b) Katritzky, A. R.; Zakaria, Z.; Lunt, E. *J. Chem. Soc., Perkin Trans. 1* **1980**, 1879−1887.

(24) The structure of F_Q^{PP} was also partially solved but due to its poor quality, the related data are not discussed and only an ORTEP drawing of the molecular entity (Figure S3) is provided in Supporting Information.

(25) Similar assignment also holds for analogous 1N,2,4,6-tetraarylpyridiniums bearing a (substituted) phenyl group at the 1N position instead of the pyridyl(ium) fragment, see (a) Kharlanov, V. A.; Knyazhansky, M. I. *J. Photochem. Photobiol. A* **1999**, *125*, 21−27. (b) Knyazhansky, M. I.; Kharlanov, V. A.; Tymiansky, Ya. R. *J. Photochem. Photobiol. A* **1998**, *118*, 151−156. (c) Knyazhanskii, M. I.; Tymyanskii, Y. R.; Feigelman, V. M.; Katritzky, A. R. *Heterocycles* **1987**, *26*, 2963−2982.

(26) This finding that biaryl spacers behave as better electron-donating groups than (methyl-substituted) monoaryl spacers is further substantiated by the observation that photobiscyclization of branched EPs, which is known to be inhibited by the biphenyl pendant group due to its electron-donating character (Scheme 1),[14,15] is however successfully achieved in the representative case of a mere xylyl pendant group as model spacer (transformation of B^X into F^X; see also Supporting Information).

(27) Energy variation of the LUMO derived from electrochemical data (ca. 0.3 V/two-electron process in going from **B** to B_Q) cannot be directly compared to that computed (1-electron process) because intervening of complex structural rearrangement correlated with reduction that allows two-electron attachment (compression of potential).[16]

(28) Peltier, C.; Lainé, P. P.; Scalmani, G.; Frisch, M. J.; Adamo, C.; Ciofini, I. *J. Mol. Struct.: THEOCHEM* **2009**, *914*, 94−99.

(29) (a) Fortage, J.; Puntoriero, F.; Tuyèras, F.; Dupeyre, G.; Arrigo, A.; Ciofini, I.; Lainé, P. P.; Campagna, S. *Inorg. Chem.* **2012**, *51*, 5342−5352. (b) Indelli, M. T.; Orlandi, M.; Chiorboli, C.; Ravaglia, M.; Scandola, F.; Lafolet, F.; Welter, S.; De Cola, L. *J. Phys. Chem. A* **2012**, *116*, 119−131. (c) Weiss, E. A.; Ahrens, M. J.; Sinks, L. E.; Gusev, A. V.; Ratner, M. A.; Wasielewski, M. R. *J. Am. Chem. Soc.* **2004**, *126*, 5577−5584.

(30) Otwinowski, Z.; Minor, W. Processing of X-ray Diffraction Data Collected in Oscillation Mode. In *Methods in Enzymology*; Carter, C. W., Sweet, R. M., Eds.; Academic Press: New York, 1997; Vol. 276 (Macromolecular Crystallography, Part A), pp 307−326.

(31) Sheldrick, G. M. *Acta Crystallogr., Sect. A* **2008**, *64*, 112−122.

(32) Pavlishchuk, V. V.; Addison, A. W. *Inorg. Chim. Acta* **2000**, *298*, 97−102.

(33) Demas, J. N.; Crosby, G. A. *J. Phys. Chem.* **1971**, *75*, 991−1024.

(34) Dempster, D. N.; Morrow, T.; Quinn, M. F. *J. Photochem.* **1974**, *2*, 329−341.

(35) Frisch, M. J; et al. *Gaussian 09*; Gaussian, Inc.: Wallingford, CT, 2009.

(36) Adamo, C.; Barone, V. *J. Chem. Phys.* **1999**, *110*, 6158−6170.

(37) Dunning, T. H., Jr.; Hay, P. J. In *Modern Theoretical Chemistry*; Schaefer, H. F., III, Ed.; Plenum: New York, 1976; Vol. 3, pp 1−28.

(38) (a) Tomasi, J.; Mennucci, B.; Cammi, R. *Chem. Rev.* **2005**, *105*, 2999−3093. (b) Marenich, A. V.; Cramer, C. J.; Truhlar, D. G.; Guido, C. A.; Mennucci, B.; Scalmani, G.; Frisch, M. *J. Chem. Sci.* **2011**, *2*, 2143−2161.